LAWRENCE
LIVERMORE
NATIONAL
LABORATORY

LLNL-JRNL-414671

Advances in NLTE Modeling for Integrated Simulations

H. A. Scott, S. B. Hansen

July 10, 2009

High Energy Density

This work performed under the auspices of the U.S. Department of Energy by Lawrence Livermore National Laboratory under Contract DE-AC52-07NA27344.

LLNL-JRNL-414671

Advances in NLTE Modeling for Integrated Simulations

H.A. Scott*
Lawrence Livermore National Laboratory, Livermore, CA 94550

S.B. Hansen
Lawrence Livermore National Laboratory, Livermore, CA 94550
Sandia National Laboratories, Albuquerque, NM 87185

Abstract

The last few years have seen significant progress in constructing the atomic models required for non-local thermodynamic equilibrium (NLTE) simulations. Along with this has come an increased understanding of the requirements for accurately modeling the ionization balance, energy content and radiative properties of different elements for a wide range of densities and temperatures. Much of this progress is the result of a series of workshops dedicated to comparing the results from different codes and computational approaches applied to a series of test problems. The results of these workshops emphasized the importance of atomic model completeness, especially in doubly excited states and autoionization transitions, to calculating ionization balance, and the importance of accurate, detailed atomic data to producing reliable spectra.

We describe a simple screened-hydrogenic model that calculates NLTE ionization balance with surprising accuracy, at a low enough computational cost for routine use in radiation-hydrodynamics codes. The model incorporates term splitting, $\Delta n=0$ transitions, and approximate UTA widths for spectral calculations, with results comparable to those of much more detailed codes. Simulations done with this model have been increasingly successful at matching experimental data for laser-driven systems and hohlraums.

Accurate and efficient atomic models are just one requirement for integrated NLTE simulations. Coupling the atomic kinetics to hydrodynamics and radiation transport constrains both discretizations and algorithms to retain energy conservation, accuracy and stability. In particular, the strong coupling between radiation and populations can require either very short timesteps or significantly modified radiation transport algorithms to account for NLTE material response. Considerations such as these continue to provide challenges for NLTE simulations.

Keywords: Non-LTE; Radiation Transport
* *E-mail address*: hascott@llnl.gov

1. Introduction

The capability to accurately model the properties of matter under non-local thermodynamic equilibrium (NLTE) conditions is critical to the ability to understand a wide variety of laboratory and astrophysical plasmas. NLTE simulations are routinely used for calculating the evolution of plasmas produced in inertial confinement fusion (ICF), magnetic fusion and other laboratory experiments, as well as to simulate spectra for diagnosing the state of these systems. Consequently, much effort has gone into developing the capability to perform these simulations and the state of the art has improved considerably over the last several years. We report here on a further advancement in this field that builds upon this body of work.

Simulating a NLTE system is a non-trivial task. The basis for most NLTE simulations is the collisional-radiative (CR) model [1], which describes each atomic system in terms of a number of atomic levels. The distribution of atomic populations among the levels is calculated by solving a set of coupled rate equations whose generation requires calculating all transition rates among the atomic levels. Most commonly, the transitions included are those mediated by collisions with electrons and photons. Material properties - opacities, emissivities, specific energies and other equation of state information - then follow from the population distributions.

For simple systems containing only a few electrons, it is feasible to enumerate each atomic level individually in terms of its configuration, fine structure state, or even as magnetic sublevels. However, the number of such levels increases exponentially with the complexity of the atomic system, even considering states with only a single electron excited out of a single shell. Figure 1 shows the total statistical weight of only these states (up to a maximum principal quantum number of 10), plus the statistical weight of a more reasonable set of states for calculating ionization balance, as a function of the number of electrons. In practice, we need to include multiple excitations from multiple shells, and a complete enumeration - even at the level of configurations - quickly becomes infeasible.

Matching the states with atomic data (energy levels, oscillator strengths, collision strengths, etc.) is another formidable task, particularly for a large complex atomic system. Fortunately, the development of codes like HULLAC [2] and FAC [3] has provided an avenue for obtaining accurate data for both atomic structure and transitions. It is now feasible to calculate data for systems comprised of up to $\sim 10^6$ levels. However, even this size pales in comparison to the number of detailed states required to model a modest atomic system.

Given the unfriendly combinatorics, the questions of which (or how many) states and transitions to include in an atomic model, and what degree of averaging to use, are critical. The answers, even given the constraints of a particular application, are not obvious and a minimal set will vary with the specific conditions. However, a very encouraging amount of progress has been made over the last decade, due partly to a series of NLTE workshops [4-8]. Participants in these workshops compared results of

calculations for a series of test cases, with the goal of understanding the most important aspects for modeling atomic systems.

As an example of the progress (and challenges) in this area, we focus on Au, which is of particular importance in ICF. At temperatures relevant to ICF, Au remains a complex M- and N-shell system which has proved challenging to model. Figure 2 shows the average ionization state <Z> of Au as a function of temperature at electron densities of 1-3 x 10^{20} cm^{-3}, as calculated by codes at the 1st and 4th NLTE workshops [4,7]. Analyzing the very large spread of results produced at the 1st workshop led to an understanding of the critical role of autoionization in high-Z systems. Incorporating sufficient doubly excited states also improved the agreement between different codes. By the 4th workshop, the most detailed codes were in quite reasonable agreement with each other. In addition, when experimental data became available [9,10], those codes were in agreement with the data. We take this result as an indication that the approach being used is sound, the atomic data is calculable, and the overall problem is tractable, although computationally very expensive.

The question of affordability is often critical, because for many applications the NLTE equations must be solved together with the equations of hydrodynamics and radiation transport. Given the computational cost of a detailed CR model, it is not surprising that integrated simulations, i.e. radiation-hydrodynamic simulations which calculate NLTE material properties in-line, tend to use much simpler models. The XSN package [11], based on an average-atom approach, has been heavily used in the ICF program at LLNL. XSN models the entire atomic system with a handful of levels (and a correspondingly small number of transitions) and is fast enough for in-line use. However, its accuracy is severely limited.

Incorporating the insights provided by the NLTE workshops, we have successfully developed a method for constructing atomic models that are compact and inexpensive enough for routine use in integrated simulations while providing accuracy comparable to far more detailed models, i.e. within the uncertainty defined by the range of detailed models. This includes both gross material properties such as ionization balance and energy density and spectral properties such as opacity and emissivity. While the truth of this statement is somewhat application dependent, the comparisons we have done support the view that the accuracy of the NLTE calculations is no longer the limiting factor in the accuracy of the integrated simulations.

The following section describes the basic method of constructing an atomic model and includes observations on the importance of various features of the model. Details of the construction and formulas used are relegated to the Appendix. The basic model presented in this section is sufficient for calculating gross material properties, but is insufficient to provide realistic spectral properties and is therefore not suitable for radiation transport simulations. Section 3 describes extensions to the model that improve the treatment of bound-bound transitions and substantially alleviate this shortcoming.

Providing an accurate, yet affordable, atomic model is a necessary but not sufficient requirement for integrated simulations. Algorithms that can handle far-from-LTE situations in radiation-hydrodynamics codes are another requirement. Simulating NLTE physics imposes additional requirements on algorithms, ranging from managing the large amount of data used to describe the state of the material to stably handling the effects of very fast atomic timescales. We discuss the impact of the latter on radiation transport calculations in section 4, and demonstrate that with current algorithms, these timescales can restrict simulation timesteps to unacceptably low values. We give one example of an algorithm, suitable for hot dense plasmas, which can ameliorate this effect.

Multiple computer codes were used for the research described in this paper. Much of the work was done with Cretin [12], a NLTE atomic kinetics / radiation transport code. In particular, the approach to generating atomic models was developed in Cretin, with significant assistance from participation in and participants from the NLTE workshops. The approach was then incorporated into the (pre-existing) DCA package in LASNEX, which was used for the radiation-hydrodynamics simulations. The two codes produce comparable atomic data, and results presented from either code will be labeled "DCA". For comparisons with a more detailed code (beyond those done as part of the NLTE workshops) we use SCRAM [13,14], with atomic data generated by FAC [3].

2. Atomic Model Construction

The two components of atomic data required for an atomic model are the atomic structure and the transition rates. Aspects of each of these have proven to be critical to adequately capturing the essential physics of non-LTE atomic kinetics. However, a high degree of accuracy in either the structure or the rates is not a critical requirement for calculating ionization balance and energetics. We describe here how we generate the atomic data and comment on the importance of various aspects of the data.

Underlying the approach we use to generate the atomic data is the screened-hydrogenic model. In this model, screening coefficients are used to calculate effective charges experienced by each bound electron. The screened charges are then used in hydrogenic formulas to construct energy levels and transition rates. This approach dates back to the work of Mayer [15] and has been applied and expanded by numerous others. Several sets of screening coefficients are available in the literature [16-19]. Faussurier [19] provides a good discussion of the theoretical basis of a screened-hydrogenic model. In practice, the sets that we have tried all give very similar results when used as described here.

We construct atomic levels as superconfigurations or Layzer complexes by populating shells described by principal quantum numbers. The energies obtained from the screening coefficients are scaled within a given isoelectronic sequence to match tabulated ionization potentials between sequences [20]. The scaling factors, which vary between 0.9 and 1.1 for most sequences but become smaller near closed shells and for near-neutral sequences, correct for some of the systematic inaccuracies of the scaled-

hydrogenic energies and significantly improve the resulting energy levels. Even with these corrections, the method does not produce highly accurate transition energies. However, it has proven to be sufficiently accurate for many non-spectroscopic applications. In addition, it allows for rapid generation of levels - possibly with multiple excitations from a combination of shells - and has allowed us to investigate the importance of different types of levels. In practice, we have found that 10-20 levels per sequence, including single and double excitations from the valence shell and excitations from lower-lying shells, is usually sufficient to match results obtained by much more detailed codes.

In most cases, the total population is distributed over only a handful of isosequences, and the range of isosequences will change slowly over the course of a simulation. We can then restrict the number of levels used in an atomic kinetics calculation at any point in time to ~100-200 levels. The computational expense is roughly an order of magnitude greater than XSN.

The model can be extended to incorporate angular momentum quantum numbers by using the screening coefficients of Faussurier [19]. However, this additional degree of description results in very much larger numbers of levels than those obtained with principal quantum numbers only. There are possible advantages to be gained here in calculating spectral properties, but at a greatly increased cost.

The most critical aspect for the atomic structure is completeness, defined here as including sufficient numbers and types of levels to incorporate all important channels for population fluxes. For systems with just a few bound electrons, a handful of singly excited states in each sequence will likely be sufficient to calculate the ionization balance. As the number of occupied shells increase, the energy differences between singly excited and doubly excited states decrease. The large statistical weights of doubly excited states make these increasingly important as the number of bound electrons increases, particularly since many of these states are autoionizing. For example, the important case of Au under ICF conditions can have multiple electrons in the N-shell. In this case, singly excited states overlap in energy with doubly excited states, and also with excitations from the M-shell. Fluxes through each of these types of states can influence the ionization balance.

Incorporating a given transition is only possible if both the initial and final states are present in the model. This rather obvious statement can lead to a significant expansion of the number of levels included in an atomic model, as it implies connections between iso-sequences. Any excited state must participate in ionizing transitions to the neighboring sequence or it will erroneously accumulate population, resulting in a skewed ionization distribution. This is particularly important at closed shells, where the valence shell of one sequence corresponds to an inner shell of the neighboring sequence and some transitions are prohibited due to the filled shell. Ensuring a continuous population flow between sequences requires avoiding these bottlenecks, while including enough states to capture the important population fluxes will then converge the population distribution.

Other states may be important for a given application, even if they do not directly affect the ionization balance - particularly when radiative properties are considered. For instance, calculating absorption of high-energy photons requires K-shell transitions for all sequences in a model. Including all these states, plus connected states, can greatly increase the size and expense of an atomic model. Fortunately, states that do not accumulate population but are required for important transitions need not engender a large number of connected states. They can even be eliminated from the atomic structure by defining compound transitions that incorporate the channel through the now-virtual states. An alternative description is that these states are algebraically eliminated from the rate matrix under the assumption that their population is always negligible.

Given the atomic structure, we then obtain transition rates from simple formulas using the appropriate screened charges. In most cases, for radiative excitations we use only hydrogenic oscillator strengths (corrected for screening) for allowed dipole transitions. The simple semi-classical formula by More [21] based on screened charges produces oscillator strengths that match quantum mechanical calculations quite well. The difference between screened and unscreened oscillator strengths usually does not significantly affect ionization balance. Collision cross-sections (or rate coefficients) are obtained from fits to the data of Sampson and Golden [22]. Alternatively, the expressions for collisional excitations and ionizations of Van Regemorter [23] or Mewe [24] and Lotz [25], respectively, can be used - again with little effect on ionization balance.

In many cases, particularly for mid- to high-Z elements, the most critical rates are those for autoionization. Bauche *et al* [26] review autoionization and resonant capture, and discuss approximations for calculating these rates. Here, following the lead of Chung *et al* [27], we use the formulation developed by Sobel'man *et al* [28]. As shown in [27], this simple formula reproduces the results of detailed calculations very well. This result, combined with the ability to generate an atomic structure that includes autoionizing states, is perhaps the key piece in inexpensively calculating ionization balance for complex atoms. It is also the most problematic part of an average-atom treatment such as XSN [29].

An example of the results obtained with this approach is given in Figure 3, which shows the average ionization state <Z> of Au as a function of temperature at an electron density of 10^{21} cm^{-3}. This extends Figure 2 to include results for higher temperatures as calculated by codes at the 5^{th} NLTE workshop [8]. The solid colored curves show results from our model (labeled DCA) and from XSN both with and without a treatment of autoionization. The solid black curves show results from the most mature detailed codes at the NLTE workshops. At low temperatures, population fluxes through the interleaved M- and N-shells are important. At high temperatures, excitation-autoionization is the dominant ionization channel. These features are modeled with comparable accuracy by the detailed codes and by our treatment, but are modeled poorly by XSN, resulting in dramatically different ionization states.

The ionization state of Au for these conditions is of more than academic interest, as it can impact the performance of targets for the National Ignition Facility (NIF). Ablation from Au hohlraum walls produces material in this density regime with temperatures of order 1-2 keV. The radiative properties and energetics of this material play an important role in the power balance within the hohlraum. Using a modified version of XSN whose rates were adjusted to produce approximately the same ionization balance and radiative emission as SCRAM and Cretin in the hohlraum, 1-D simulations showed a reduction of about 20% in the laser power required to achieve a desired capsule drive. The differences are attributable to the higher emissivity of the more accurate models, which leads to a lower ionization state and smaller energy density in the ablated material [30].

3. Extensions to Atomic Models for Radiation Transport

The atomic model described so far calculates ionization balance and energetics very well for optically thin material, but falls short when used to drive radiation transport for optically thick material. This is because the amount of radiation absorbed and emitted in optically thin material is independent of line profiles and insensitive to line positions, while optically thick radiation transport depends critically on these quantities. The highly averaged transitions in an atomic model described solely by principal quantum numbers do not carry sufficient information to provide reasonable opacity and emissivity spectra. However, extending the atomic model with a relatively small amount of information accounts for the most important missing details and improves the spectra considerably.

There are two extensions to the treatment of radiative excitations in the model that improve the spectra. The first is to split each photoexcitation transition between principal quantum numbers into multiple term-to-term transitions with individual energies and oscillator strengths. For example, an n=2 $\rightarrow$ n=3 transition becomes the following set of transitions: 2s+ $\rightarrow$ 3p-, 2s+ $\rightarrow$ 3p+, 2p- $\rightarrow$ 3s+, 2p- $\rightarrow$ 3d-, 2p+ $\rightarrow$ 3d-, and 2p+ $\rightarrow$ 3d+. We use tabulated energy levels and oscillator strengths which have been calculated with the LIMBO code [31] for singly excited states up to n=7 for each element and isosequence. This provides more accurate transition energies and oscillator strengths than can be achieved with the screened-hydrogenic model alone, and more importantly, provides a realistic spread of transition energies. In practice, we have found that splitting photoexcitations for transitions involving shells up to a couple above the valence shell (not necessarily up to n=7) is sufficient to achieve good results with only a modest increase in computational expense.

An additional benefit of the term splitting is the improved treatment of $\Delta n=0$ transitions, which become increasingly important to the radiative properties of M- and N-shell systems. For models based on principal quantum numbers, these transitions have previously been handled with averaged transition energies and oscillator strengths, calculated under coronal conditions [32]. This data represents these transitions poorly under more general conditions and cannot easily be extended. The current treatment improves this situation considerably, providing very good opacity spectra from these transitions. The corresponding emission spectra are somewhat dependent on the precise

implementation, which requires a method for estimating the relative term populations within a shell, but are vastly improved over the previous treatment.

This term-splitting procedure improves the transition energies and general shape of n $\rightarrow$ n' transition complexes for singly excited states, but does not distinguish between transition complexes from singly and doubly excited levels. That distinction can be recovered by applying an energy shift (obtained from the hydrogenic transition energies) to the LIMBO term-to-term transition energies, giving rise to satellite complexes that yield even better agreement with detailed codes. In the interest of computational efficiency, this satellite extension is not used in the DCA results presented here, but is used for supplemental transitions in the hybrid-model SCRAM calculations described below.

The second extension assigns an additional width to each transition, representing additional unresolved fine structure multiplets, modeling each transition as an unresolved transition array (UTA). The formulation we use combines a simple empirical formula to approximate UTA widths and a multiplier intended to decrease the broadening when the density drops low enough so that the multiplet levels are no longer collisionally coupled. Specifically, for a transition energy dE in an ion of charge Q = Z – (# of bound electrons), the additional broadening ΔE is given by

$$\Delta E = f\varepsilon \ , \ \varepsilon = \min (dE/3,\ Q) \qquad (1)$$

where the multiplier f is given by

$$f \ = \ \min \left(1. \ , \ 1.3\text{x}10^{-13} \frac{n_e e^{-\varepsilon/T}}{T^{1/2}\varepsilon^3} \right) \qquad (2)$$

Alternatively, f can be defined in terms of the statistical weight g_0 of the ground-level valence shell n (or ground-state term nlj) and the occupancy N of that shell (or term) for the transition's lower level: $f = \min(N, g_0\text{-}N)/g_0$. Instead of changing to reflect collisional coupling, this definition gives broader features for open-shell ions under any plasma conditions and broadens in response to density through the increasing population of multiply excited states. It is especially useful in increasing the fidelity of calculated spectra when using the energy shift for multiply excited satellite lines mentioned above.

Figure 4 demonstrates the effects of these extensions on the opacity of optically thin Fe, at a temperature of 800 eV and electron density of 10^{22} cm^{-3}. In the extended treatment, additional L-shell transitions appear between 1 and 2 keV, and the multiple n$\rightarrow$n+1 transitions below 1 keV are no longer resolved. Most importantly for radiation transport, the peak opacities of the strong transitions decrease due to the splitting and broadening.

A comparison of results from this model to that of a much more detailed code is given in Figure 5, which shows emission spectra for optically thin Xe at a temperature of 4 keV and an electron density of $3.6\text{x}10^{20}$ cm^{-3}. The detailed spectrum was calculated with SCRAM, using hybrid atomic data [14] constructed from a combination of fine structure and UTA data from FAC, supplemented with the extended screened-hydrogenic model (including satellite shifts). The agreement is excellent, both in mean ionization <Z> and

in the emission spectrum.

In our experience, this extended model provides surprisingly accurate opacity and emissivity spectra over a range of materials and conditions - as measured by comparisons with detailed calculations. However, the cases for which detailed calculations are available are quite limited. Experimental verification is difficult, as integrated experiments tend to have uncertainties due to multiple physical processes. However, we describe two experiments where the results of LASNEX simulations using the current atomic models with DCA match measured data significantly better than simulations performed with XSN.

The first case comes from a series of joint LLNL/CEA experiments performed on the Omega laser in which Au-plated spheres were illuminated with various laser pulses [33]. Figure 6 shows the first few ns of the emitted X-ray flux in the 2-3 keV band resulting from a 10 kJ, 3 ns, 10^{14} W/cm^2 pulse. The figure also shows the results of LASNEX simulations using XSN and DCA. The DCA results show a qualitative improvement in the increased early time emission. Quantitative agreement is still less than satisfactory. However, the results depend heavily on other physical processes (laser absorption, hydrodynamics, radiation transport, electron transport). The origin of the remaining disagreement is as yet unknown.

The situation is clearer for the second experiment. Ge-doped aerogel foam targets were irradiated with the Omega laser, and X-ray yields were measured for a variety of targets and laser pulses [34]. The spectral band from 0-3 keV includes Ge L-shell emission while the band from 9-11 keV includes Ge K-shell emission. A simulation using DCA gives a total energy emitted in the lower band of 4.7 kJ, compared to ~4.2-4.4 kJ measured. In the upper band, the simulation gives a total energy emitted of 135 J, compared to ~113-126 J measured. For this simulation, the critical computational model for matching the measurements is the treatment of non-local thermal conduction [35]. Simulations with XSN give a K-shell emission no more than half of what is measured, independent of the thermal conduction model.

4. Algorithms for NLTE Radiation Transport

The extended screened-hydrogenic model described in the previous two sections provides accurate equation of state and radiative properties for NLTE plasmas, but that is only one requirement for successful integrated NLTE simulations. Algorithms that can handle far-from-LTE situations are another requirement. Radiation transport algorithms, in particular, require modification to remain stable and accurate. When radiation transports significant energy, the numerical formulation is desired to be implicit in time for both intensity and temperature, as the difference between absorption and emission determines the change in material temperature. For LTE, Kirchoff's law states that the emission divided by absorption (i.e. the source function) is a Planckian at the material temperature, and that relationship is used to produce an implicit treatment of material properties. Under NLTE conditions, the relationship between the temperature, intensity

and emission spectrum is not known apriori. In addition, the operative timescales are even shorter, as the emission (and absorption) can change on very fast atomic timescales due to changes in radiation intensity as well as temperature. The result is that a standard transport algorithm applied to a NLTE situation can easily become unstable, or just produce inaccurate results.

As an example, we consider a 0-D Au plasma at a density of 0.2 g/cm^3 and a temperature of 0.3 keV, initially in equilibrium with zero radiation field. We introduce a Planckian radiation field with radiation temperature T_R = 2 keV and calculate the response of the plasma. The plasma will heat due to absorption of radiation until emission balances absorption, leaving the material at a temperature of 2 keV. Figure 7 shows the evolution of the material temperature, calculated implicitly with a standard Newton-Raphson algorithm (utilizing the temperature derivatives of the material energy density, emissivity and opacity) for initial timesteps ranging from 10^{-16} to 10^{-10} sec. All timesteps result in the material equilibrating at the correct temperature, but the evolution is grossly inaccurate (and physically unreasonable) for timesteps much larger than 10^{-15} sec. The algorithm fails because it is not actually implicit in intensity, having neglected the strong dependence of the material properties - primarily the emission - on the intensity.

Although this example uses a high-Z material and a large radiation field (both appropriate to ICF), the underlying issue is more general and can be demonstrated for a wide range of materials and conditions. If the radiation intensity significantly affects the material properties, then the transport algorithm must either be implicit or resolve the timescale on which the material responds. The difference from the LTE case is that the material properties depend explicitly on the radiation intensity (and time) and can change even if the temperature remains constant. In addition, the strong coupling between line radiation and populations can produce changes on very fast atomic timescales.

A better algorithm attempts to be implicit in intensities and temperatures by re-evaluating the material properties using updated temperatures and intensities. A single iteration improves the results for this 0-D example dramatically. Figure 8 compares the temperature evolution for initial timesteps of 10^{-14}, 10^{-12} and 10^{-10} sec. for both the standard algorithm and an algorithm that re-evaluates material properties before each temperature update. The iterative algorithm – with a single iteration – produces evolution tracks that are essentially independent of timestep, achieving the desired implicit behavior. However, this approach does not account for changes in intensity due to non-local effects, and becomes unstable for optically thick systems. A generalized transport algorithm designed to be implicit in both temperatures and intensities [36] can remain stable and accurate, but is not yet computationally feasible.

The fundamental problem here is the absence of an NLTE analogue to Kirchoff's law to relate the emission, absorption, temperature and intensity. To bypass this problem, we propose an ansatz for the source function S_ν of the following form:

$$S_\nu = \frac{\left(r_\nu^0 - e^{-\beta x^0}\right) + \left(1 - r_\nu^0\right) e^{-\beta x}}{\left(1 - e^{-\beta x^0}\right)} B_\nu \tag{3}$$

where B_ν is the Planckian, the superscript "0" denotes the values at the beginning of the timestep, and

$$r_\nu^0 = \frac{S_\nu^0}{B_\nu^0} \ , \ x = \frac{h\nu}{kT} \tag{4}$$

This ansatz is based on the expectation that at low frequencies (small values of x), the emission will be Planckian. The functional form assumes an exponential approach to Planckian emission, quantified by the free parameter β. For material dense enough for energy levels within a few kT to be collisionally coupled, β is expected to be of order ~1/few.

We apply this ansatz to an optically thick version of the 0-D example, i.e. a gold slab 20 cm. thick illuminated by a 2 keV radiation field. Figure 9 displays the temperature evolution at different positions within the slab for a standard radiation transport algorithm using temperature derivatives as calculated by the atomic kinetics (dashed lines) and for the same algorithm modified to use the ansatz. The unmodified algorithm suffers from severe stability problems and never produces a reasonable spatial profile for the material temperature, while the modified algorithm evolves smoothly and produces the same temperature profile as a simulation using extremely small timesteps. Further work in this area will attempt to assess the impact and accuracy of this type of approach to NLTE radiation transport.

5. Summary

The capability to model NLTE atomic systems has improved greatly over the last decade, and has reached the stage where quite complex ions can be addressed with some measure of success. This progress is very encouraging, but the computational expense of the best treatments and most detailed codes is formidable.

Building upon the insights and results of the detailed codes, we have produced a method for constructing highly-averaged atomic models that, in many cases, provide results of comparable accuracy to detailed models at a computational cost low enough for inclusion in radiation-hydrodynamic codes. The basic method, distinguishing atomic states solely on the basis of principal quantum numbers, provides surprisingly accurate calculations of ionization balance. Adding term splitting and simple approximate UTA widths for photoexcitations produces emission and absorption spectra suitable for driving radiation transport calculations. It is now likely that, in many cases, the accuracy of NLTE calculations is no longer limiting the overall fidelity of the integrated simulations.

There remain serious issues with numerical treatments of radiation transport in highly NLTE situations. Current methods may not remain stable and accurate under these

conditions, and we have presented one candidate algorithm suitable for hot dense plasmas. Much work remains to be done on this topic in the future.

Acknowledgments

The authors are grateful to Brian Wilson for providing data from the LIMBO code, to Mordy Rosen, Larry Suter, and Jeff Colvin for sharing the results of their hydrodynamic simulations, and to the participants in the NLTE code comparison workshops for valuable discussions and insight.

This work was performed under the auspices of the U.S. Department of Energy by Lawrence Livermore National Laboratory under Contract DE-AC52-07NA27344. SH was partially supported by Sandia, a multiprogram laboratory operated by Sandia Corporation, a Lockheed Martin Company, for the U.S. Department of Energy under Contract No. DE-AC04-94AL85000.

Appendix: Formulas for Atomic Models

The formulas presented here form the basis for the atomic models discussed in section 2.

Energy levels:

The screened-hydrogenic energy for level i is evaluated as

$$E_i = \Re \sum_n P_n \frac{Q_n^2}{n^2}\left(1 + \alpha^2 \frac{Q_n^2}{n^2}\left[\frac{2n}{n+1} - \frac{3}{4}\right] + \frac{\alpha^4}{6}\frac{Q_n^4}{n^4}\right) \quad \text{(A1)}$$

where P_n is the occupation number for the shell of principal quantum number n and α is the fine structure constant. Here, $\Re$ is the Rydberg constant,

$$\Re = \frac{2\pi^2 m e^4}{h^2} = 13.6 \ \ eV \quad \text{(A2)}$$

with e the electron charge, m the electron mass (or the appropriate reduced mass), and h the Planck constant. The factors proportional to powers of α are the first two relativistic corrections, which become significant for large nuclear charge Z. The screened charges Q_n are obtained from

$$Q_n = Z - \sum_{m<n} \sigma_{nm} P_m - \tfrac{1}{2}\sigma_{nn}(P_n - 1) \quad \text{(A3)}$$

where σ_{nm} are the screening constants. This formulation is based on principal quantum numbers only, and for the screening constants given in [16,17], only inner electrons ($m \le n$) screen the nucleus. For the screening constants given in [18,19], which also depend on the orbital angular momentum quantum number l, outer electrons ($m > n$) also contribute to the screening. In this case, the factor in square brackets changes to $[2n/(l+1) - ¾]$.

The energies derived in this manner are quite accurate for highly-charged atomic systems with only a few electrons and moderately accurate for many atomic systems, but lose accuracy for closed-shell and near-neutral systems. We correct for some of the

systematic inaccuracies by applying scaling factors that force ground state ionization energies to match those obtained from detailed calculations [20]. Specifically, the scaling factor $s(I)$ for isosequence I is defined as

$$s(I) = \frac{E_{tab}(I) - E_{tab}(I-1)}{E_g(I) - E_g(I-1)} \tag{A4}$$

where E_{tab} is the tabulated result and E_g is the screened-hydrogenic energy for the ground state of the isosequence. For excited states i within isosequence I, the corrected energy $\tilde{E}_i$ is then

$$\tilde{E}_i = E_{tab}(I) + s(J)\left[E_i - E_g(I)\right]. \tag{A5}$$

For excitations out of shells with n=3 or above, we apply the scaling factor for the current isosequence (I=J). For excitations out of the two innermost shells, we apply the scaling factor for the isosequence J appropriate to those shells.

Transition data:

The data necessary for calculating transition rates is obtained from the formulas given below. Because each shell n contains P_n identical electrons, the appropriate data for a transition $n \rightarrow m$ contains both an availability factor P_n and a blocking factor $(1-P_m/2m^2)$.

For oscillator strengths f_{nm} for dipole transitions, we use hydrogenic values with a screening correction consistent with the semiclassical formula of More [21]. Kramers' approximation for hydrogenic values [37],

$$f_{nm}^{hyd} = \frac{32}{3\pi\sqrt{3}} \frac{nm^3}{(m^2-n^2)^3} \tag{A6}$$

is quite accurate for large values of n, and we supplement this with tabulated values for small n. By comparison with the semiclassical formula,

$$f_{nm}^{sc} = \frac{32}{3\pi\sqrt{3}} \frac{Q_n^4 Q_m^2}{n^5 m^3} \left(\frac{\Re}{E_m - E_n}\right)^3 \tag{A7}$$

we adopt the formula

$$f_{nm} = f_{nm}^{hyd} \left[\left(\frac{Q_n}{Z}\right)^4 \left(\frac{Q_m}{Z}\right)^2 \left(\frac{Z^2\Re}{E_m - E_n}\right)^3 \left(\frac{1 + {(\alpha Z)^2}/{n^2}}{n^2} - \frac{1 + {(\alpha Z)^2}/{m^2}}{m^2} \right)^3 \right] P_n \left(1 - \frac{P_m}{2m^2}\right)$$

where the factor in square brackets is the screening correction. Note that the screening correction must be calculated with unscaled energies, while all other formulas in this section use scaled energies.

Photoionization cross sections are obtained from Kramers' formula [37], using screened charges in place of the nuclear charge. For the ionization of an electron of principal quantum number n by a photon of energy $h\nu$, the cross section is given by

$$\sigma_\nu = \frac{32}{3\pi\sqrt{3}} \left(\frac{\pi e^2}{mc}\right) \frac{Q_n^4}{n^5} \left(\frac{\Re}{h\nu}\right)^3 g_{bf} P_n \tag{A8}$$

where g_{bf} is the bound-free Gaunt factor of Karzas and Latter [38]. Although this

formula was derived for a hydrogenic ionization threshold of $(Q/n)^2\,\Re$, we use the threshold energy obtained from the scaled energies when calculating rates.

Data for collisional rates can come from different sources. We first discuss collisional excitation for the transition $n \rightarrow m$. The expression for the cross-section is often written in terms of the oscillator strength in a form based upon the Bethe approximation

$$\sigma_{nm} = \frac{8\pi}{\sqrt{3}} \pi a_0^2 \left(\frac{\Re}{E_{nm}} \right)^2 \frac{g(x)}{x} f_{nm} \tag{A9}$$

where $E_{nm}=E_m-E_n$, $x=\varepsilon/E_{nm}$, ε is the electron energy, and $g(x)$ is the Gaunt factor. The rate coefficient is then obtained by integrating over the electron distribution F_e,

$$C_{nm} = \int_{E_{nm}}^{\infty} \mathrm{v}(\varepsilon)\sigma_{nm}(\varepsilon)F_e(\varepsilon)d\varepsilon \tag{A10}$$

where $\mathrm{v}(\varepsilon)$ is the electron velocity. Various authors have proposed expressions for Gaunt factors, the simplest of which is the constant value $g(x) = 0.2$ suggested by Van Regemorter [23] for near-threshold electron energies, which can be integrated analytically for a Maxwellian electron distribution. The form suggested by Mewe [24], $g(x) = A + B/x + C/x^2 + D\,ln(x)$, also leads to an analytic expression for the rate coefficient. For allowed transitions, he recommends using A=0.15, B=0, C=0, D=0.28, matching Bethe's form for the Born approximation.

Collisional ionization rates can be approached in a similar manner. A simple expression comes from the work of Lotz [25], who used a cross-section for ionization out of state n that can be put in the form

$$\sigma_n = \frac{8\pi}{\sqrt{3}} \pi a_0^2 \left(\frac{\Re}{E_n} \right)^2 \frac{g(x)}{x} \tag{A11}$$

where E_n is the ionization energy and $x=\varepsilon/E_n$. He adopted a semi-empirical Gaunt factor with leading term $g(x) = A\,ln(x)$, with values for A in the range of 0.13 - 0.17 for ionization out of most shells.

Sampson and Golden [22] adopted a different approach to the Gaunt factor. Their semi-empirical choice, which also depends on ionization threshold and nuclear charge, was designed to provide continuity between excitation and ionization cross-sections, with coefficients determined by matching experimental results and Coulomb-Born calculations. They provide moderately complex expressions for Gaunt factors for both excitation and ionization, and for the resulting Maxwellian rate coefficients. For computational efficiency, we adopt fits to their Gaunt factors obtained by Zimmerman [39], which allow straightforward evaluation of cross-sections or Maxwellian rate coefficients.

For autoionization rates, we use the method of Chung *et al* [27]. These rates involve three states – the autoionizing state n, plus the lower and upper states i,j from the next ionized isosequence that provide a stabilizing transition. The autoionization rate A is given by

$$A = \frac{64\pi}{\sqrt{3}} \frac{Q_i^2}{n^3} \frac{g_i}{g_n} \frac{\Re^2}{hE_{ij}} f_{ij} g(E_{ij}) P_j (1 - \frac{P_i}{2i^2})(1 - \frac{P_n}{2n^2}) \quad \text{(A12)}$$

where g_i is the statistical weight of state i and $g(E)$ is the Gaunt factor. The Gaunt factor used here is a constant, $g = 0.12$, and the oscillator strength f_{ij} includes screening but no availability or blocking factors, as these are displayed explicitly.

References

[1] D.R. Bates, A.E. Kingston and R.W.P. McWhirter, Proc. R. Soc. **A267**, 297 (1962).
[2] A. Bar-Shalom, M. Klapisch and J. Oreg, J. Quant. Spectros. Radiat. Transfer **71**, 169 (2001).
[3] M.F. Gu, Astrophys. J. **590**, 1131 (2003).
[4] R.W. Lee, J.K. Nash, and Y. Ralchenko, J. Quant. Spectrosc. Radiat. Transf. **58**, 131 (1997).
[5] C. Bowen, A. Decoster, C.J. Fontes, *et al*, J. Quant. Spectrosc. Radiat. Transf. **81**, 71 (2003).
[6] C. Bowen, R.W. Lee and Yu. Ralchenko, J. Quant. Spectros. Radiat. Transfer **99**, 102 (2006).
[7] J. Rubiano, R. Florido, C. Bowen, *et al*, High Energy Density Physics **3**, 225 (2007).
[8] C.J. Fontes, J. Abdallah Jr., C. Bowen, *et al*, High Energy Density Physics **5**, 15 (2009).
[9] M.E. Foord, S.H. Glenzer, R.S. Thoe, *et al.*, Phys. Rev. Letters **85**, 992 (2000).
[10] R.F. Heeter, S.B. Hansen, K.B. Fournier, *et al.*, Phys. Rev. Letters **99**, 195001 (2007).
[11] W.A. Lokke and W.H. Grasberger, UCRL-52276, Lawrence Livermore National Laboratory, Livermore, CA (1977).
[12] H.A. Scott, J. Quant. Spectros. Radiat. Transfer **71**, 689 (2001).
[13] S. Hansen, PhD dissertation, University of Nevada, Reno (2003).
[14] S. Hansen, J. Bauche, C. Bauche-Arnoult and M.F. Gu, High Energy Density Physics **3**, 109 (2007).
[15] H. Mayer, LA-647, Los Alamos Scientific Laboratory, Los Alamos, NM, (1947).
[16] R.M. More, J. Quant. Spectros. Radiat. Transfer **27**, 345 (1982)
[17] R.M. Marchand, S. Caille and Y.T. Lee, J. Quant. Spectros. Radiat. Transfer **43**, 149 (1990).
[18] F. Perrot, Physica Scripta **39**, 332 (1989).
[19] G. Faussurier, C. Blancard and A. Decoster, J. Quant. Spectros. Radiat. Transfer **58**, p. 233 (1997).
[20] J. Scofield, private communication.
[21] R. More, in *Handbook of Plasma Physics* **3**, (eds. A.M. Rubenchik and S. Witkowski), 63 (1991).
[22] D.H. Sampson and L.B. Golden, Astrophys. J. **170**, 169 (1971).
[23] H. Van Regemorter, Astrophys. J. **136**, 907 (1962).

[24] R. Mewe, Astron. Astrophys. **20**, 215 (1972).
[25] W. Lotz, Zeitschrift Phys. **216**, 241 (1968) and **220**, 266 (1969).
[26] J Bauche, C Bauche-Arnoult, and O. Peyrusse, High Energy Density Physics **5**, 51 (2009).
[27] H.-K. Chung, M.H. Chen, W.L. Morgan, *et al*, High Energy Density Physics **1**, 3 (2005).
[28] I.I. Sobel'man, L.A. Vainshtein and E.A. Yukov, *Excitation of Atoms and Broadening of Spectral Lines*, 2nd. Ed., Springer, Berlin (1995).
[29] J.R. Albritton and B.G. Wilson, J. Quant. Spectros. Radiat. Transfer **65**, 1 (2000).
[30] L.J. Suter, presented at Atomic Processes in Plasmas, Monterey (2009).
[31] D.A. Liberman, J.R. Albritton, B.G. Wilson, W.E. Alley, Phys. Rev. A **50**, 171 (1994).
[32] D.E. Post, R.V. Jensen, C.B. Tarter, *et al*, Atom. Data and Nucl. Data Tables **20**, 397 (1977).
[33] M.D. Rosen, H.A. Scott, L.J. Suter, S.B. Hansen, presented at APS Division of Plasma Physics, Dallas (2008).
[34] K.B. Fournier, J.H. Satcher, M.J. May, *et al*, Phys. Plasmas **16**, 052703 (2009).
[35] J. Colvin, in preparation.
[36] H.A. Scott, High Energy Density Physics **1**, 31 (2005).
[37] H.A. Kramers, Philos. Mag. **46**, 836 (1923).
[38] W. Karsaz and R. Latter, Ap. J. Suppl. **6**, 167 (1961).
[39] G. Zimmerman, private communication.

Figure Captions

Fig. 1 Total statistical weight for ground state and excited states including principal quantum numbers up to n=10 as a function of isosequence. The solid line includes singly excited states from the valence shell only. The dashed line also includes a moderate number of doubly excited states plus states with inner-shell excitations. The trend is exponential growth with dips around closed shells.

Fig. 2 Average ionization state <Z> as a function of temperature for Au with no radiation field as calculated by codes at the 1st NLTE workshop (dashed lines) and 4th NLTE workshop (solid lines). The electron density was 10^{20} cm^{-3} for the 1st workshop and 3 x 10^{20} cm^{-3} for the 4th workshop. The experimental data points (markers) are from [6] and [7], with estimated electron densities of 6-14 x 10^{20} cm^{-3}.

Fig. 3 Average ionization state <Z> as a function of temperature for Au with no radiation field as calculated by codes at the 4th NLTE workshop (dashed lines for T≤5 keV) and 5th NLTE workshop (dashed lines for T≥6 keV)). The electron density was 3 x 10^{20} cm^{-3} for the 4th workshop and 10^{21} cm^{-3} for the 5th workshop. The thin solid curves show results from the detailed codes at the workshops. The experimental data points (markers) are the same as in Fig. 2. The other solid curves gives results from DCA (middle curve) and XSN, both with autoionization / dielectronic recombination (bottom curve) and without autoionization / dielectronic recombination (top curve).

Fig. 4 Opacity as a function of photon energy for Fe at a temperature of 800 eV with an electron density of 10^{22} cm^{-3}. The light curve shows the opacity as calculated by the basic screened-hydrogenic model described in the text, with n→n' transitions. The dark curve shows the opacity as calculated by the extended model, with term-to-term transitions.

Fig. 5 Emissivity as a function of photon energy for Xe at a temperature of 4 keV with an electron density of 3.6 x 10^{20} cm^{-3}. The light curve shows the emissivity as calculated by SCRAM. The dark curve shows the emissivity as calculated by DCA. Calculated ionization states are given in the legend.

Fig. 6 Total radiative flux from photons with energies between 2-3 keV as a function of time from an Au-coated sphere illuminated with a 10 kJ, 3ns, 10^{14} W/cm^2 pulse from the Omega laser. The top curve gives the experimental results. The dashed (dotted) curves give simulation results obtained using DCA (XSN). Only the first couple ns of the emission are shown.

Fig. 7 Temperature as a function of time for a 0-D Au plasma of initial temperature 0.3 keV and density 0.2 g/cm^3 illuminated by a 2 keV blackbody. The curves correspond to different initial timesteps, ranging from 10^{-16} sec to 10^{-10} sec.

Fig. 8 Temperature as a function of time for the same case as Fig. 7 for initial timesteps of 10^{-14}, 10^{-12} and 10^{-10} sec. The curves marked with small crosses are the same as in Fig. 7 (including an initial timestep of 10^{-16} sec). The curves marked with circles show the results obtained with the iterative algorithm described in the text. They are difficult to distinguish because they coincide for most time points.

Fig. 9 Temperature as a function of time for different positions within a 20 cm Au slab of initial temperature 0.3 keV and density 0.2 g/cm^3 illuminated by a 2 keV blackbody. The dotted lines show simulation results using a standard radiation transport algorithm. The solid lines show simulation results using the ansatz described in the text.

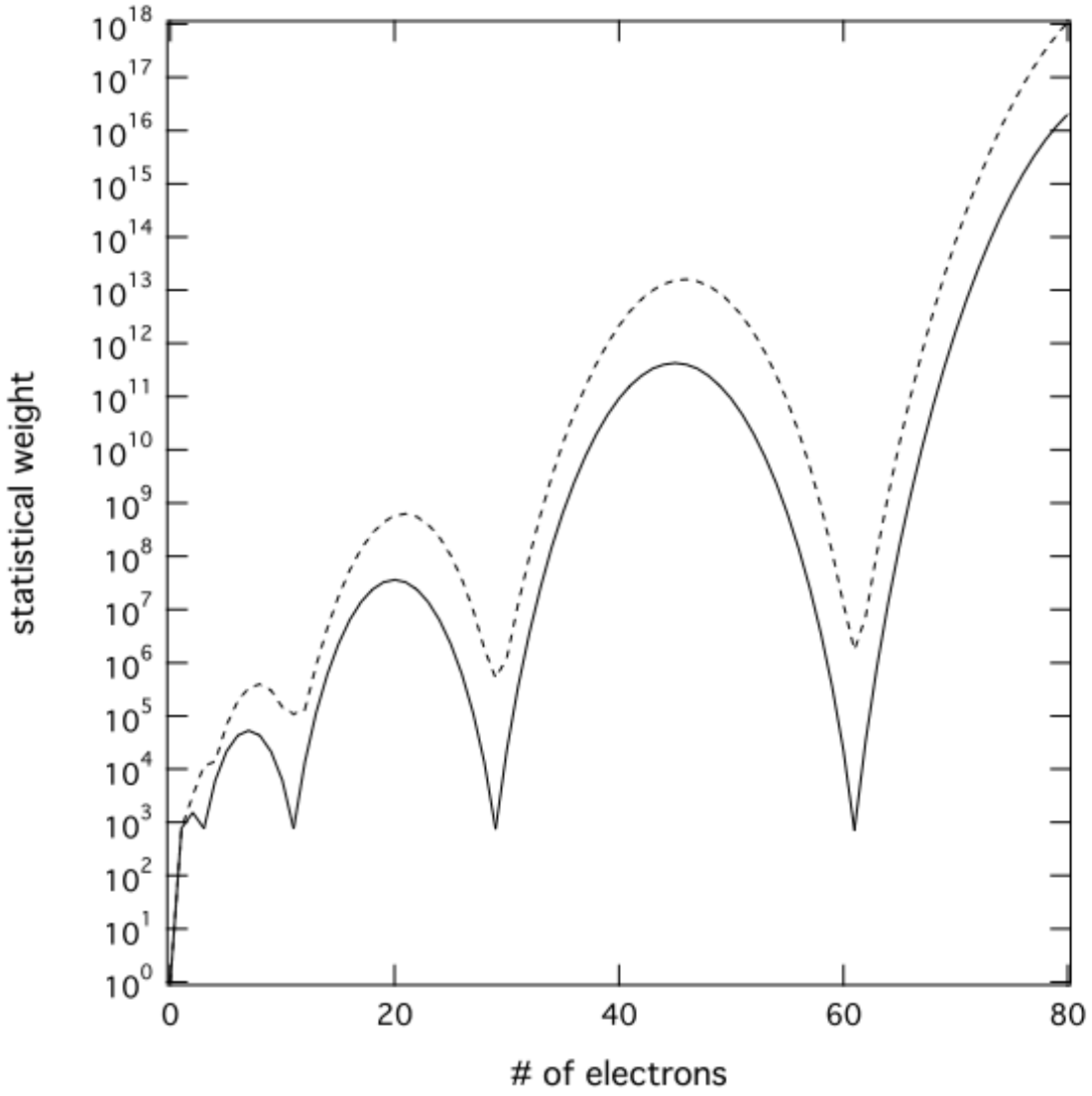
statistical weight
10^{18}
10^{17}
10^{16}
10^{15}
10^{14}
10^{13}
10^{12}
10^{11}
10^{10}
10^{9}
10^{8}
10^{7}
10^{6}
10^{5}
10^{4}
10^{3}
10^{2}
10^{1}
10^{0}
0
20
40
60
80
# of electrons

Figure 1

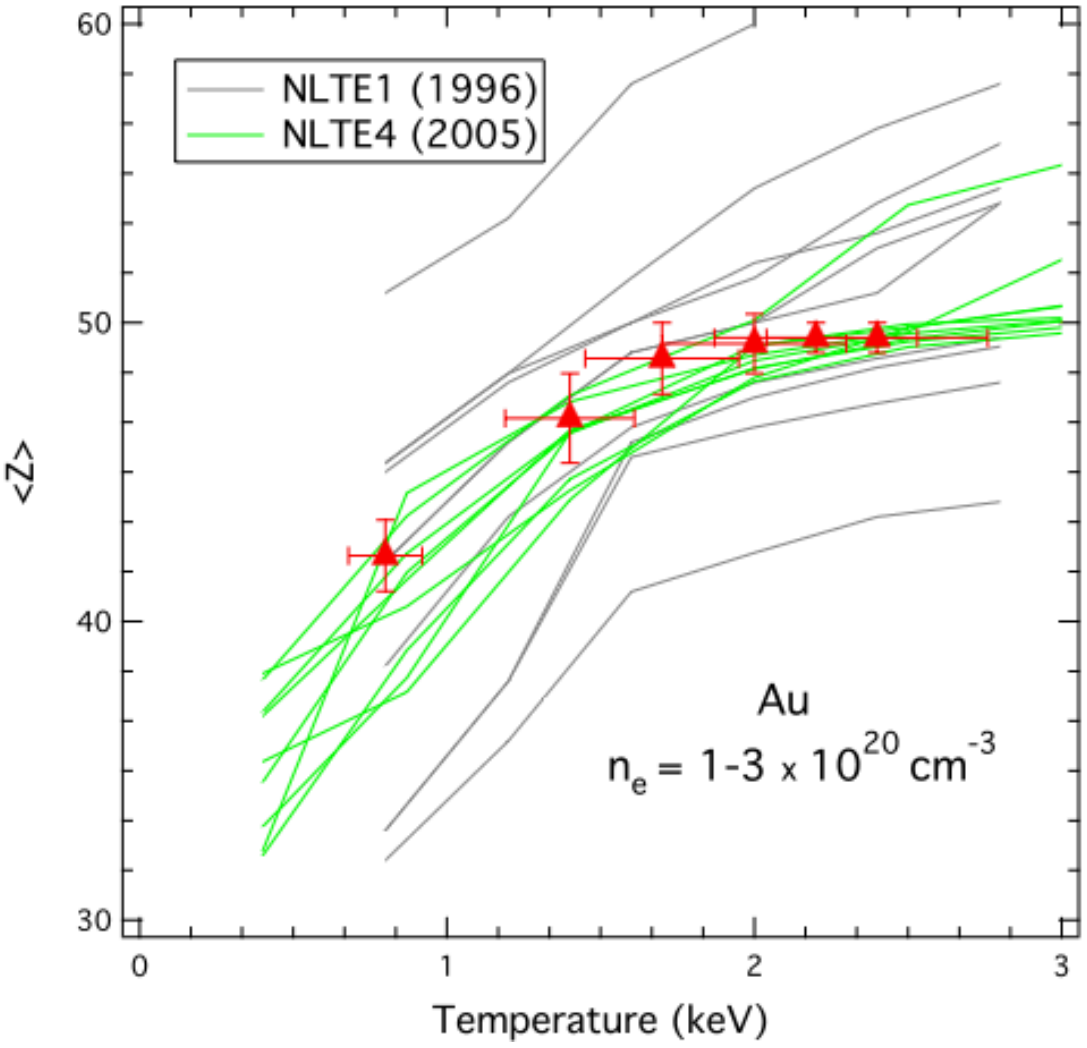
NLTE1 (1996)
NLTE4 (2005)
Au
n_e = 1-3 x 10^{20} cm^{-3}
<Z>
Temperature (keV)
60
50
40
30
0
1
2
3

Figure 2

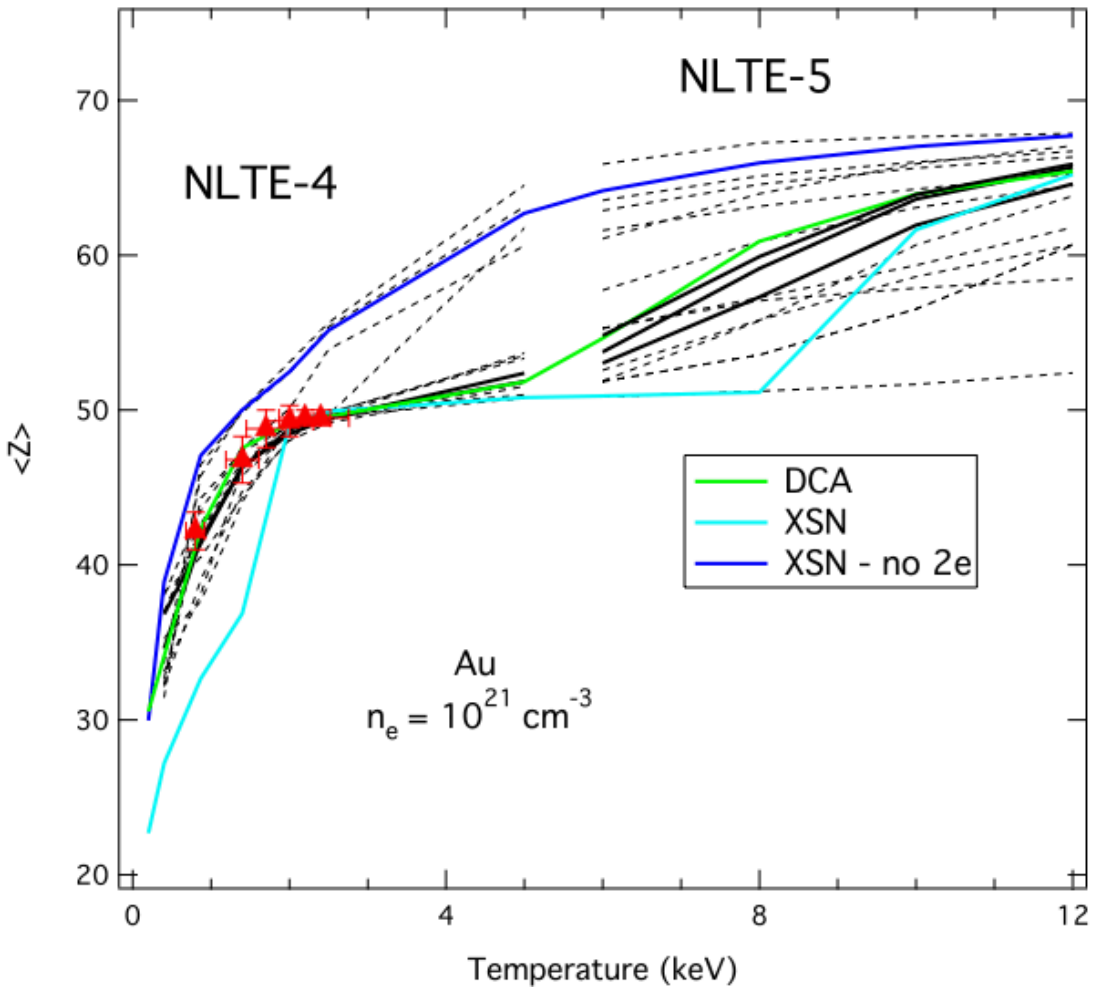
NLTE-5
NLTE-4
70
60
50
40
30
20
<Z>
0
4
8
12
Temperature (keV)
DCA
XSN
XSN - no 2e
Au
$n_e = 10^{21}$ cm^{-3}

Figure 3

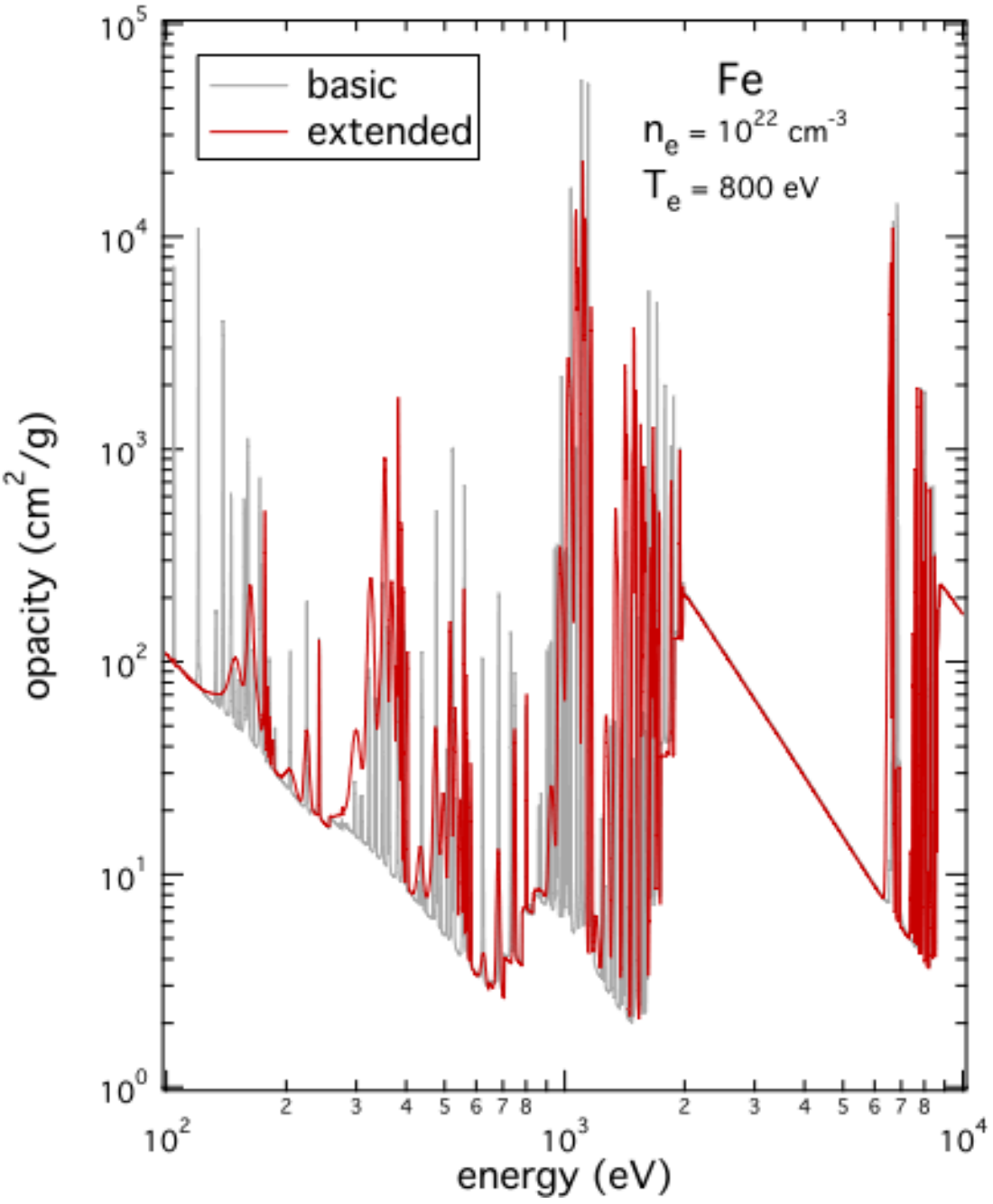
basic
extended
Fe
$n_e = 10^{22}$ cm^{-3}
T_e = 800 eV
opacity (cm^2/g)
energy (eV)
10^0
10^1
10^2
10^3
10^4
10^5
10^2
10^3
10^4
2 3 4 5 6 7 8
2 3 4 5 6 7 8

Figure 4

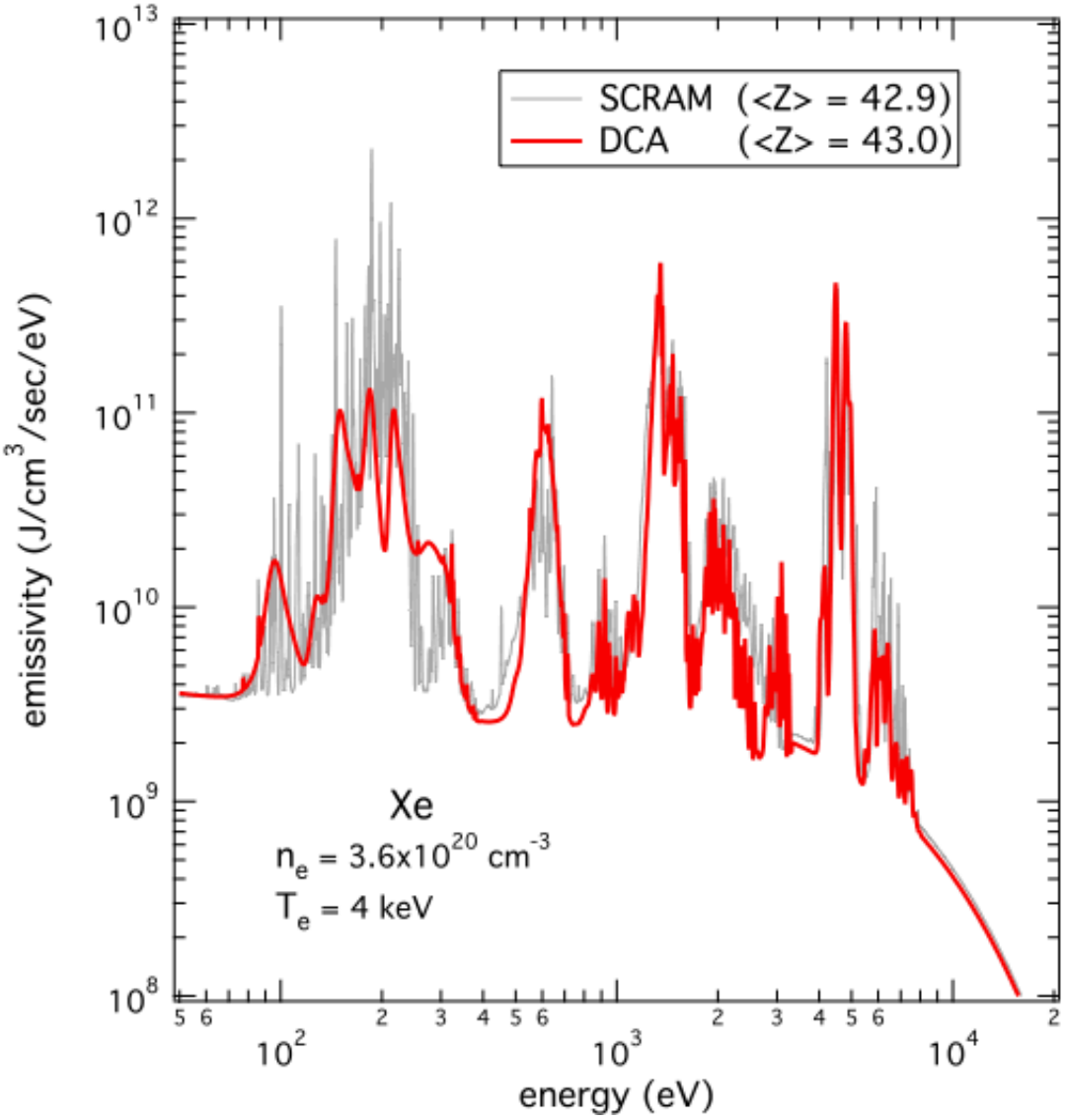
SCRAM (<Z> = 42.9)
DCA (<Z> = 43.0)
Xe
$n_e = 3.6 \times 10^{20}$ cm^{-3}
T_e = 4 keV
emissivity (J/cm^3/sec/eV)
energy (eV)

Figure 5

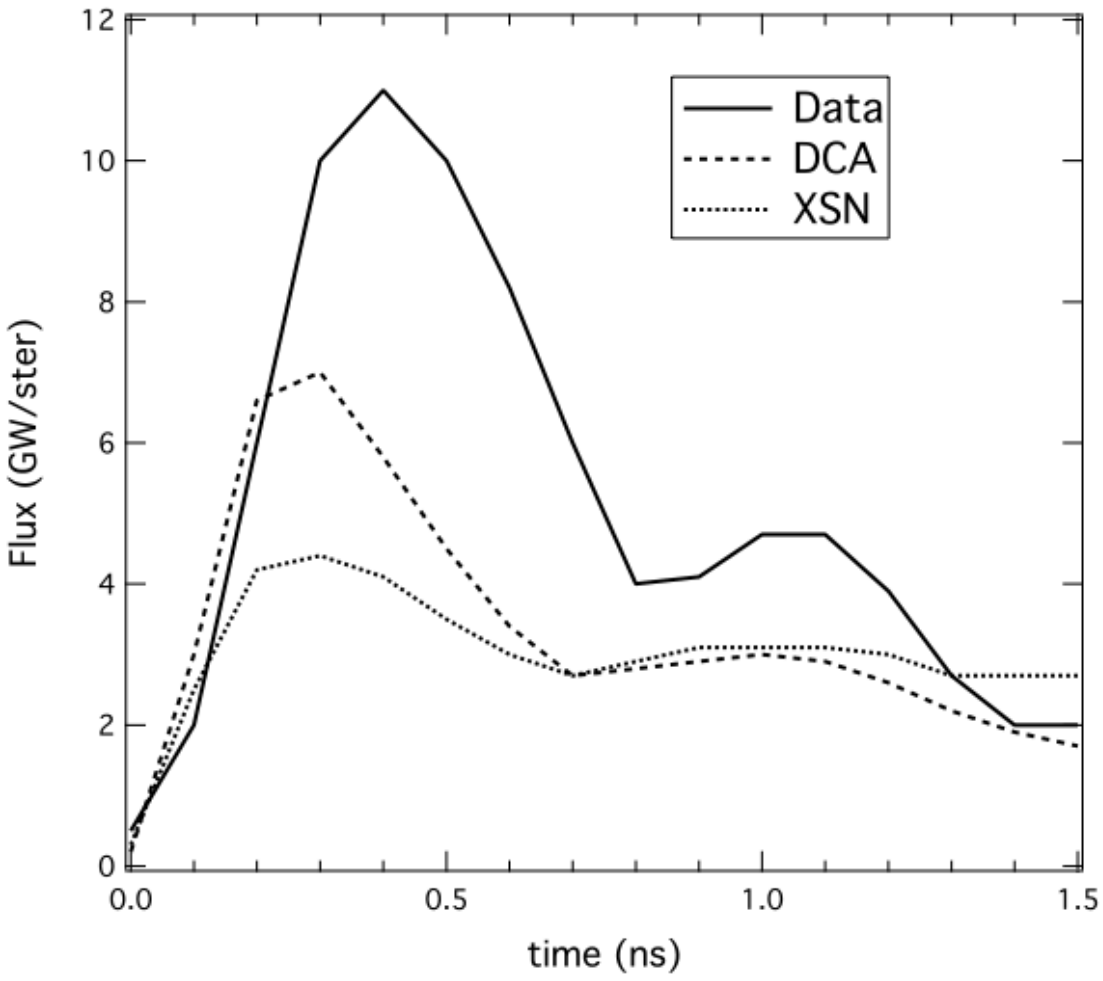

Figure 6

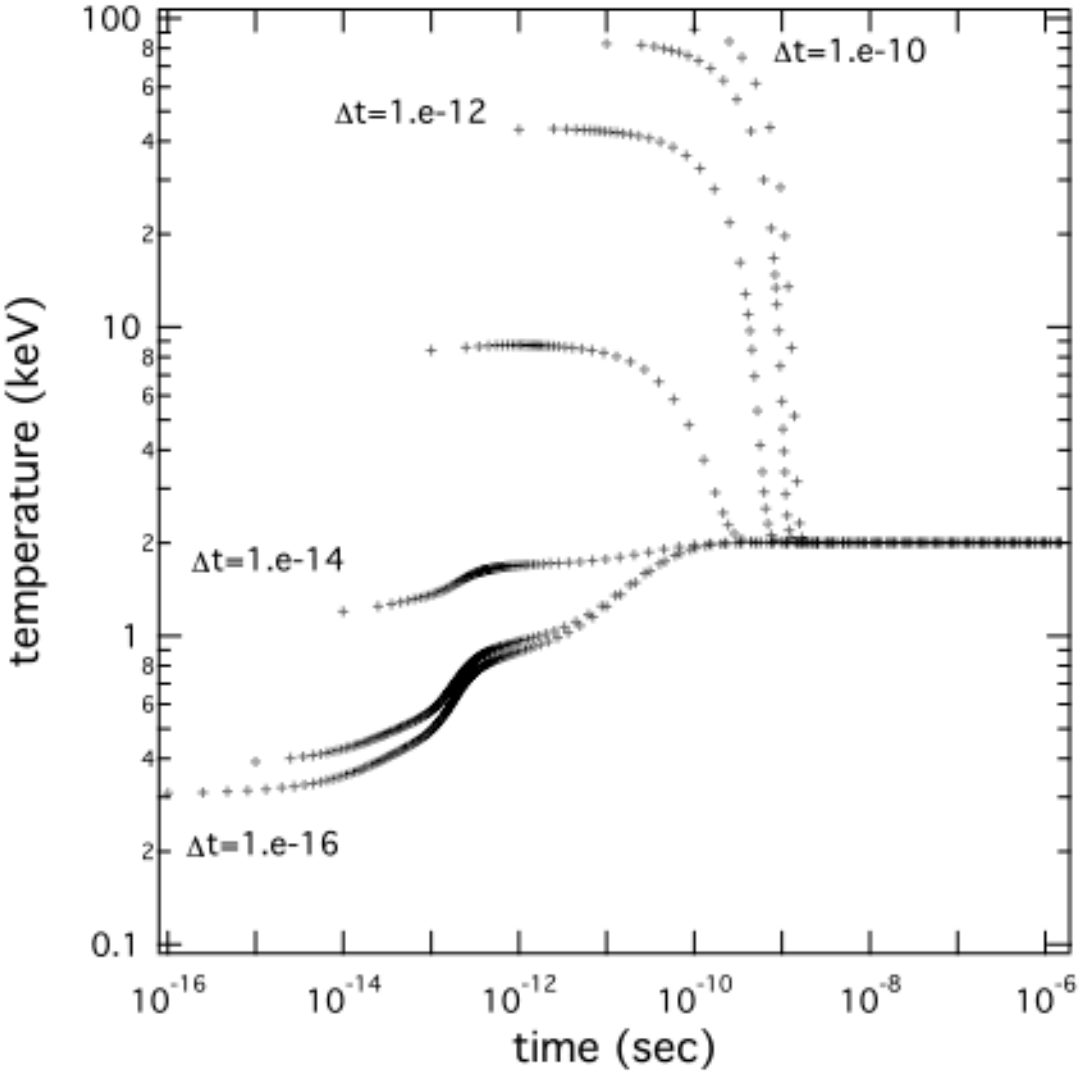
temperature (keV)
time (sec)
Δt=1.e-10
Δt=1.e-12
Δt=1.e-14
Δt=1.e-16
100
10
1
0.1
10^{-16}
10^{-14}
10^{-12}
10^{-10}
10^{-8}
10^{-6}

Figure 7

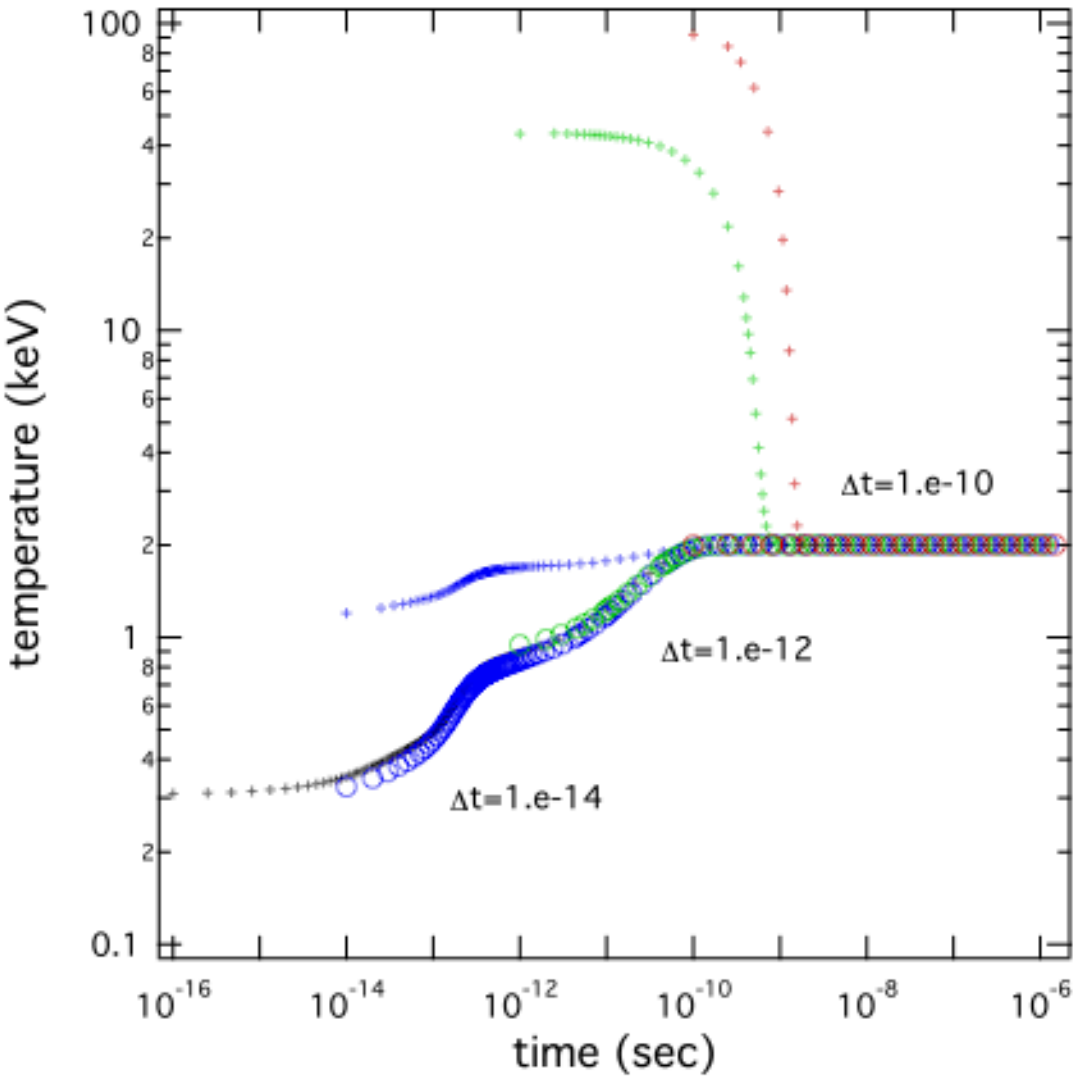
temperature (keV)
time (sec)
100
10
1
0.1
10^{-16}
10^{-14}
10^{-12}
10^{-10}
10^{-8}
10^{-6}
Δt=1.e-10
Δt=1.e-12
Δt=1.e-14

Figure 8

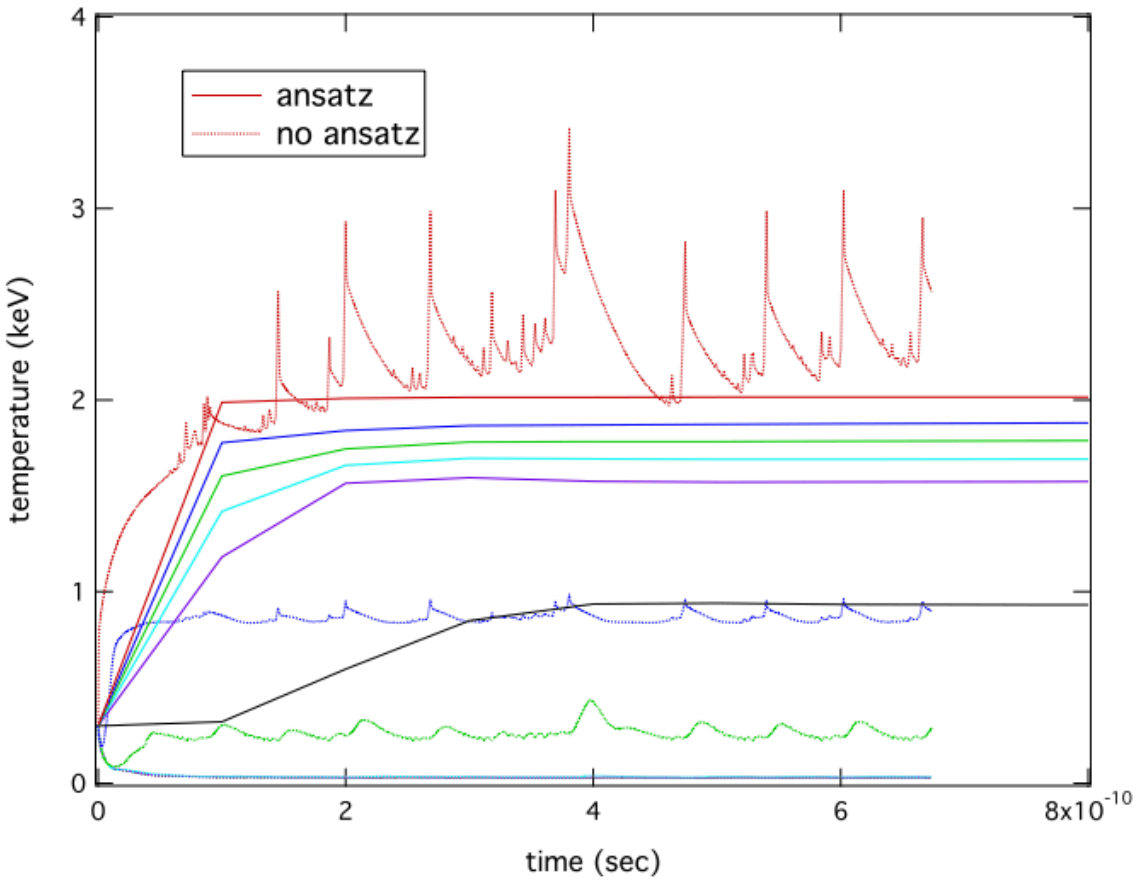
ansatz
no ansatz
temperature (keV)
time (sec)
0
1
2
3
4
0
2
4
6
8x10^-10

Figure 9